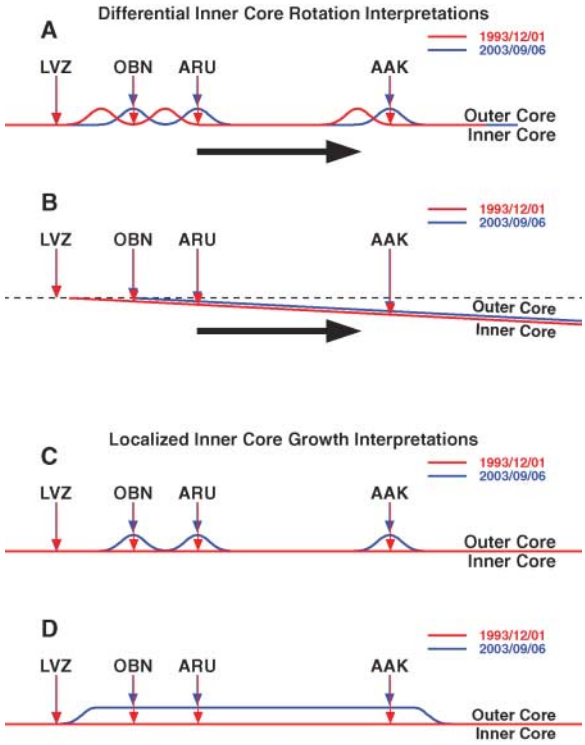


**Fig. 4.** Illustration of possible scenarios to change the inner core boundary at PKiKP reflected points between the occurring times of the doublet. (**A** and **B**) The inner core boundary has irregular topography and is changed by a differential inner core rotation. The dashed line in (B) is the equilibrium position of the inner core boundary. (**C** and **D**) The inner core boundary is changed by rapid localized inner core growth.


5. G. F. Davies, Paper 10/30, *XVII General Assembly. IUGG*. Canberra (1979).
6. D. E. Loper, P. H. Roberts, *Phys. Earth Planet. Int.* **24**, 302 (1981).
7. D. J. Stevenson, T. Spohn, G. Schubert, *Icarus* **54**, 466 (1983).
8. B. A. Buffett, in *Earth's Deep Interior: Mineral Physics and Tomography from the Atomic to the Global Scale*, S.-I. Karato *et al.*, Eds., Geophysical Monograph **117**, 37, American Geophysical Union, Washington, DC (2000).
9. S. Yoshida, I. Sumita, M. Kumazawa, *J. Geophys. Res.* **101**, 28085 (1996).
10. D. R. Fearn, D. E. Loper, P. H. Roberts, *Nature* **292**, 232 (1981).
11. D. J. Stevenson, *Geophys. J. R. Astron. Soc.* **89**, 311 (1987).
12. J. Zhang *et al.*, *Science* **309**, 1357 (2005).
13. G. Poupinet, A. Souriau, O. Coutant, *Phys. Earth Planet. Int.* **118**, 77 (2000).
14. G. Poupinet, W. L. Ellsworth, J. Frechet, *J. Geophys. Res.* **89**, 5719 (1984).
15. D. P. Schaff, P. G. Richards, *Science* **303**, 1176 (2004).
16. A. Y. Li, P. G. Richards, *Geochem. Geophys. Geosys.* **4**, 1072 10.1029/2004GL021240 (2003).
17. X. D. Song, *Phys. Earth Planet. Inter.* **124**, 269 (2001).
18. G. Poupinet, A. Souriau, *Phys. Earth Planet. Inter.* **124**, 275 (2001).
19. X. D. Song, P. G. Richards, *Nature* **382**, 221 (1996).
20. K. C. Creager, *Science* **278**, 1284 (1997).
21. J. E. Vidale, D. A. Dodge, P. S. Earle, *Nature* **405**, 445 (2000).
22. Materials and methods are available as supporting material on *Science* Online.
23. I. Sumita, P. Olson, *J. Geophys. Res.* **107**, 2169 10.1029/2001JB000548 (2002).
24. M. G. Worster, *J. Fluid Mech.* **237**, 649 (1992).
25. G. Hulot, C. Eymin, B. Langlais, M. Mandea, N. Olsen, *Nature* **416**, 620 (2002).
26. J. Bloxham, D. Gubbins, A. Jackson, *Philos. Trans. R. Soc. Lond. A* **329**, 415 (1989).
27. Time shifts in Fig. 1, B, D, and E, and Fig. 2, and travel time residuals in Fig. 3, are defined as $T^{pre}_{03-93,k,p}$ and $T^{res}_{03-93,k,p}$ in (*22*), respectively. They are estimated using the best-fitting relative origin time (6 September 2003, 15:47:00.205) and hypocenter position of event 03 (fig. S2A).


28. I thank two anonymous reviewers for constructive reviews and W.-C Yu for assistance in collecting the seismic data. This work is supported by the National Science Foundation.


**Supporting Online Material**
www.sciencemag.org/cgi/content/full/1131692/DC1
Materials and Methods
Figs. S1 to S3
Table S1
References


23 June 2006; accepted 23 August 2006
Published online 28 September 2006;
10.1126/science.1131692
Include this information when citing this paper.


# Transcrystalline Melt Migration and Earth's Mantle


**Pierre Schiano,[1]* Ariel Provost,[1] Roberto Clocchiatti,[2] François Faure[1]†**



**Plate tectonics and volcanism involve the formation, migration, and interaction of magma and gas. Experiments show that melt inclusions subjected to a thermal gradient migrate through olivine crystals, under the kinetic control of crystal-melt interface mechanisms. Exsolved gas bubbles remain fixed and eventually separate from the melt. Scaled to thermal gradients in Earth's mantle and geological times, our results account for the grain-scale segregation of primitive melts, reinterpret $CO_2$-rich fluid inclusions as escaped from melt, and question the existence of a free, deeply percolating fluid phase. Melt migration experiments also allow us to quantify crystal growth kinetics at very low undercoolings in conditions appropriate to many natural systems.**


Deciphering the physical processes by which melts (silicate-rich liquids) and "fluids" ($CO_2$- or $H_2O$-rich gases or supercritical fluids) form, migrate, and interact is necessary to fully understand the dynamics of Earth's mantle and volcanism. It has long been believed, for instance, that the migration of magma has two modes: porous flow through small channels along grain boundaries followed by flow through a fracture network. Also, melt and fluid inclusions in mantle minerals are supposed to be the direct expressions of independent, deeply percolating fluid and melt phases (*1*). Here, we present experimental results that introduce transcrystalline melt migration as a mechanism occurring in Earth and suggest that most fluid inclusions in mantle minerals represent natural remnants of transcrystalline melt migration rather than samples of a free, fluid phase that pervades the mantle.

The samples used in this study are olivine crystals collected from lapilli levels at Piton Vincendo (Piton de la Fournaise Volcano, Reunion Island, Indian Ocean) and La Sommata


[1]Laboratoire Magmas et Volcans, Observatoire de Physique du Globe, Université Blaise Pascal et CNRS, 5 rue Kessler, 63038 Clermont-Ferrand Cedex, France. [2]Laboratoire Pierre Süe, Centre d'Etudes Nucléaires de Saclay, Commissariat à l'Energie Atomique et CNRS, 91191 Gif-sur-Yvette Cedex, France.

*To whom correspondence should be addressed. E-mail: schiano@opgc.univ-bpclermont.fr

†Present address: Centre de Recherches Pétrographiques et Géochimiques, Université Henri Poincaré et CNRS, 15 rue Notre-Dame des Pauvres, 54501 Vandoeuvre-lès-Nancy, France.

(Piano Caldera, Vulcano Island, Aeolian Arc) scoria cones (*2–4*). The selected crystals contain subspherical vitreous inclusions (30 to 300 μm in diameter) consisting only of glass and a bubble containing $CO_2$, as verified by laser-Raman analyses. The distribution of inclusions is not controlled by healed fractures (as might be expected for inclusions of secondary origin), and gas bubbles readily dissolve into the melt at magmatic temperatures (which would not happen systematically if inclusions were originally multiphase). These inclusions represent droplets of the parental liquid, captured during the growth of their host crystal. Vitreous inclusions in $Fo_{83-84}$ olivine from Piton Vincendo have homogeneous, $H_2O$-poor (0.74 ± 0.07 weight %, where the error = 2 SD) alkali basalt compositions with 8.68 ± 0.60 wt % MgO and 0.68 ± 0.11 wt % $K_2O$, whereas inclusions in $Fo_{90-91}$ olivine from La Sommata have homogeneous, $H_2O$-rich (3.70 ± 0.10 wt %) basalt compositions of the shoshonitic series (10.16 ± 0.95 wt % MgO and 1.83 ± 0.26 wt % $K_2O$) (table S1).

The experiments were performed in a microscope 1-atm heating stage (*5*, *6*) and a purified He atmosphere. The oxygen fugacity was monitored in the outgoing gas flux with a zirconia probe, calibrated with an Ar + 1% $H_2$ gas, and calculated to be kept at $10^{-10}$ to $10^{-9}$ atm at 1100°C. The mean temperature was monitored with a Pt-$Pt_{90}Rh_{10}$ thermocouple directly welded to the sample holder. The temperature gradient inside the working zone (0.03 to 0.06 K/μm) was mapped by melting small pieces of gold disseminated on the olivine plate; it was further checked on each run by melting two pieces of gold placed on the extremities of the studied melt inclusion. In some experimental runs, the crystals were first heated up (52 K/min) to the temperature at which the inclusions homogenize to a single, uniform melt phase (1170° to 1230°C for La Sommata inclusions, 1200° to 1280°C for Piton Vincendo), then cooled down (30 K/min) to the temperature of bubble nucleation (about 20 to 50 K below the homogenization temperature) and maintained at these conditions for 1 to 20 hours. In other runs, the crystals were carried straight to the final temperature. We observed the same behavior regardless of procedure.

At the onset of an experiment, the fluid bubble moves toward the cold side of the working zone (this reduces free energy because gases have greater expansion coefficients than melts), reaching and wetting the inclusion cavity wall almost instantaneously (Fig. 1A). While the melt slowly and continuously shifts toward the hot side, the bubble front end is dragged by the melt, but the rear end remains motionless (Fig. 1, B to F). The bubble stretches and distorts to a dumbbell shape and a fixed, crystal-hosted bulge develops at the expense of the moving, melt-hosted bulge (Fig. 1G). The fluid is thus progressively extracted from the melt and engulfed by the host crystal. The fluid wake ultimately pinches off [possibly through dislocation creep (*7*) given that no crystal rupture is detected], leaving one or more isolated, subspherical fluid inclusions (Fig. 2, A and B). In brief, the melt migrates toward the hot spot of the working zone, leaving the fluid bubble behind, which ultimately forms a separate, motionless fluid inclusion. Segregation of fluid inclusions generally occurs after a displacement of about twice the size of the parent inclusion.

While moving, the melt inclusion gradually changes from subspherical to a faceted, negative-crystal shape (it also lengthens and narrows slightly). Indeed, this shape reveals that migration is not strictly parallel to the thermal gradient but proceeds along a small-index crystallographic direction ([001] in the case of Fig. 1). Melt migration was monitored from the bubble rear end and other fixed reference marks such as small crystal defects. Migration rate, obtained by measuring the bubble track on successive photographs, stays constant during an experiment (Fig. 3A). In La Sommata samples, migration rates varied from 1 to 3.2 nm/s for 0.03 to 0.06 K/μm thermal gradients and 1134° to 1175°C mean temperatures (Table 1). Lower migration rates were obtained for Piton Vincendo: 0.3 to 1.3 nm/s for 0.03 to 0.04 K/μm and 1190° to 1196°C.

At the end of the experiments, the samples were quenched, mounted in epoxy, and polished for microprobe analysis. Representative composition profiles are shown in fig. S1. Host olivine displays no zoning, and its composition is the same at the front, back, and sides. Although the glass of Piton Vincendo inclusions is not zoned either, La Sommata inclusions display a uniform, ~10-μm wide, outer region in which CaO content increases and MgO decreases toward the crystal wall. Otherwise, the glasses are homogeneous and compositionally similar to unheated vitreous

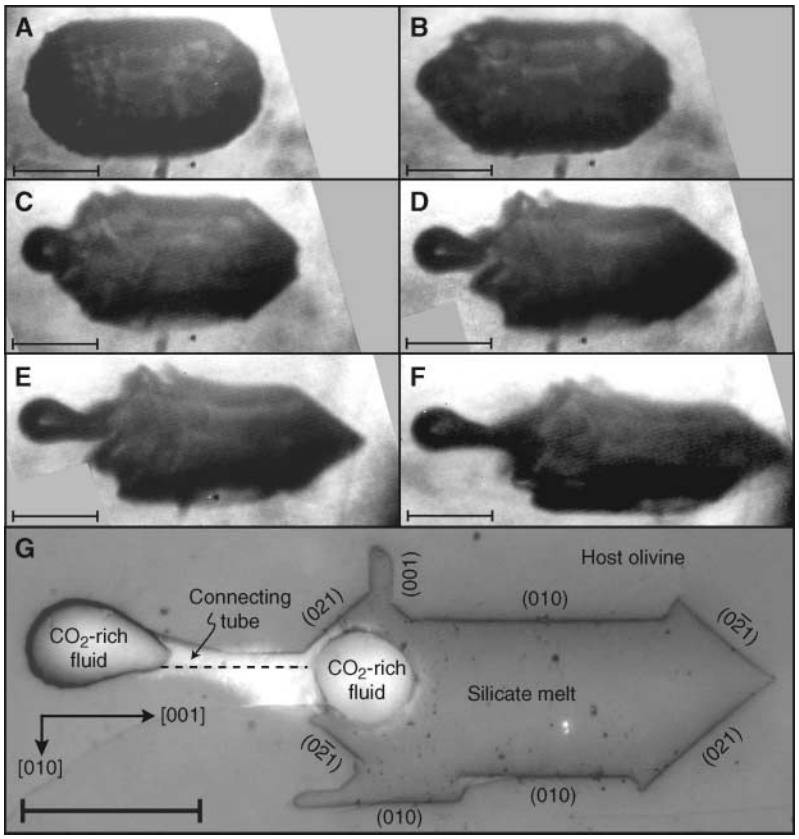


**Fig. 1.** Morphological evolution of melt-and-bubble inclusions. (**A** to **F**) Transmitted-light images of an olivine-hosted, $CO_2$-oversaturated melt inclusion during run Som1 (Table 1). Melt inclusion migrates toward the working-zone hot spot (to the right of each image, beyond the edge) and takes a faceted shape. A $CO_2$ bubble is initially hosted by the melt but wets the crystal at the inclusion cold end. It later stretches and constricts, developing a motionless, crystal-hosted bulge. (**G**) Reflected-light microphotograph of the inclusion after quenching and polishing for exposure. A thin, fluid-filled tube still connected the growing, crystal-hosted and residual, melt-hosted bulges at the end of experiment, but polishing has scraped the tube walls (one edge of the tube section, discernible on photograph enlargements, is indicated by dashes). Also shown are the crystallographic axes and Miller indices of host olivine. Scale bars, 50 μm.

inclusions from the same samples. The zoning pattern of La Sommata quenched glasses is typical of diffusion-limited crystal growth, accounting for the inward crystallization of a ~1-μm olivine layer. It is not a result of melt migration but represents a quench artifact [La Sommata melts are more difficult to quench than Piton Vincendo melts because of their lower viscosities (*8*, *9*)].

We interpreted the thermal migration of melt inclusions as due to olivine dissolution ahead and crystallization astern, because creep would not maintain a faceted shape. Inclusions are delimited by the commonly observed {021} and (010) faces of olivine (Fig. 1G), but also by the less common (001) faces at the back. Faces (001) are typical of olivine crystals showing a polyhedral habit (*10*), a morphology thought to develop during slow crystal growth governed by molecular attachment, when the uptake and rejection of chemical components at the interface of solids and liquids are slower than their diffusion in the melt (*11*). Indeed, diffusion-controlled migration would occur parallel to the thermal gradient whatever the orientation of the host crystal, whereas melt inclusions actually migrate along a low-index crystallographic direction (Fig. 1). Diffusion-limited dissolution (*12*) and crystallization would also require MgO melt content to decrease, and CaO content to increase, from front to back; microprobe analyses failed to detect concentration gradients associated with the migration, which is another indication that interface detachment and attachment are the rate-controlling processes. Given that no discernible chemical modification of the trapped melt or host olivine was observed either, inclusion volume is left constant during migration, showing that dissolution and crystallization rates are equal.

Quantitative interpretation of the observed migration rates requires a thermodynamic analysis of the process of dissolution and crystallization. For the sake of simplicity, we modeled a melt inclusion geometrically as a prism of length $L$ (30 to 130 μm) and chemically as a binary mixture of dissolved host olivine and MgO-free solvent [olivine mole fraction $\overline{C}$ = 0.203 for La Sommata samples and 0.190 for Piton Vincendo (table S2)]. Inclusion migrates by crystallizing olivine at the cooler rear end (with a temperature $T_1$ and a molar fraction $C_1$) while host olivine melts at the hotter front end ($T_2$ and $C_2$). Latent heat is transported from rear to front by conduction, and dissolved olivine travels in the other direction by diffusion. The binary diffusion coefficient $D$, taken as the self-diffusion coefficient of the slowest cation (Si), is greater than $10^{-12}$ m$^2$/s at the temperatures and compositions we studied (*13*, *14*), whereas thermal diffusivity (*15*) κ is on the order of $10^{-6}$ m$^2$/s. The time scale for attainment of steady state is $L^2/D$ = a few minutes for diffusion, and much less for conduction (i.e., boundary layers merge within minutes and the whole inclusion behaves as a diffusion layer). Migration velocity $V$ is on the order of $10^{-9}$ m/s, $VL/\kappa << VL/D < 0.1$; thus, both $T$ and $C$ steady-state profiles are linear: $T = T_1 + \theta x$ and $C = C_1 + \gamma x$, where $x$ is the distance from rear and $\theta = (T_2 - T_1)/L$, $\gamma = (C_2 - C_1)/L$. Notably, latent heat negligibly affects the imposed thermal gradient $\theta_0$: $\theta \approx \theta_0 \cos\alpha$, where α is the angle of thermal gradient and migration path ($\cos\alpha \approx 1$ in our experiments).

Migration is governed by the interplay of boundary condition $V = D\gamma/(1 - \overline{C})$ and interface kinetics $V = f(\Delta\mu)$, where Δμ is the driving force for fusion and crystallization. Function $f$ depends on the dominant interface mechanism (*11*), which could be continuous detachment and attachment, the propagation of screw dislocations, or surface nucleation [$f(u) = k_c u$, $k_s u^2$, or $k_n \exp(-a/u)$, where $k_c$, $k_s$, $k_n$, and $a$ are constants]. $\Delta\mu = \mu_{liq}(T_1,P,C_1) - \mu^0_{sol}(T_1,[\sigma]) = \mu^0_{sol}(T_2,[\sigma]) - \mu_{liq}(T_2,P,C_2)$, where $\mu^0_{sol}$ is the molar free enthalpy of host olivine; [σ] stands for the three invariants of the stress tensor, the same at both ends; and $\mu_{liq}$ is the chemical potential of the olivine component in the melt (at pressure $P$). Classical thermodynamic relations give $\Delta\mu = \Delta\mu_T - \Delta\mu_C$, where $\Delta\mu_T = ½(S^0_{liq} - S^0_{sol})\theta L$ and $\Delta\mu_C = ½R\,\overline{T}\gamma L/\overline{C}$, assuming a constant activity coefficient of the olivine component [where $S^0_{sol}$ is molar entropy of host olivine, $S^0_{liq}$ is partial molar entropy of the olivine component, $R$ is the gas constant, and $\overline{T} = ½(T_1 + T_2)$]. Equating the two expressions for $V$ fixes γ and, thus, fixes $V$. Two endmember cases appear: diffusion control $\Delta\mu << \Delta\mu_T \rightarrow V \approx V_D = D\,\overline{C}(S^0_{liq} - S^0_{sol})\theta/(1 - \overline{C})R\overline{T}$, and interface kinetics control $\Delta\mu_C << \Delta\mu_T \rightarrow V \approx V_K = f(\Delta\mu_T)$. In practice, $V \approx V_D$ if $V_D << V_K$ and $V \approx V_K$ if $V_K << V_D$. Control by chemical diffusion makes $V$ proportional to thermal gradient θ and independent of inclusion length $L$. Control by interface kinetics

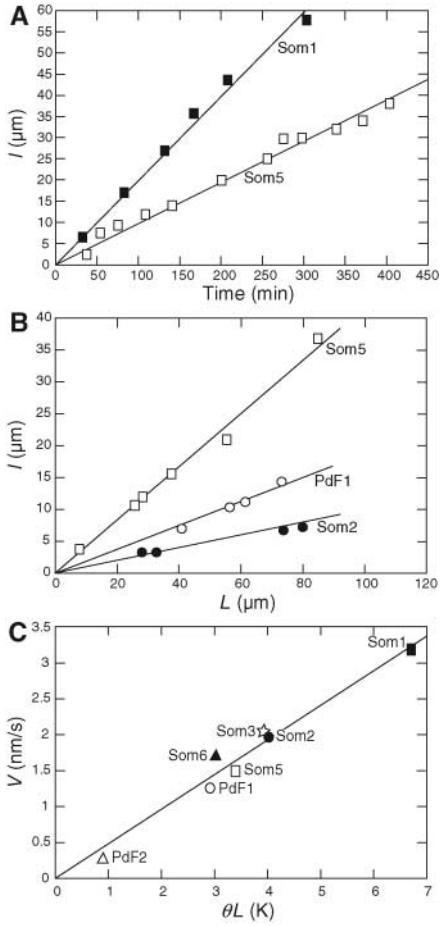


**Fig. 3.** Kinetics of transcrystalline melt migration (experimental runs Som1 to Som6, PdF1, and PdF2, see Table 1). (**A**) Bubble track length $l$ (a measure of melt migration distance) versus time, showing that migration rate is constant for a given inclusion in given experimental conditions. (**B**) Final bubble track length $l$ versus inclusion length $L$ for crystals with several melt inclusions, showing that the different inclusions of a given crystal migrate at rates proportional to their lengths. (**C**) Migration rate $V$ versus the product of thermal gradient θ and inclusion length $L$, showing that the same, linear kinetic law applies to different experimental conditions and different crystals from two different geological settings. Best-fit slope is 0.48 ± 0.07 nm s$^{-1}$ K$^{-1}$ (where error = 2 SD). $V$ does not depend only (or even mainly) on θ, as diffusion control would demand (fig. S2).

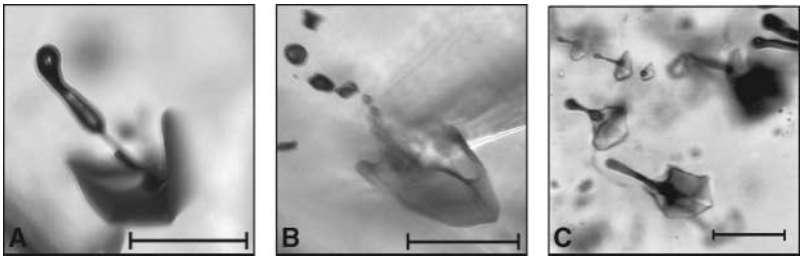


**Fig. 2.** (**A** and **B**) Transmitted-light microphotographs showing how a $CO_2$ bubble (upper left), left over by a migrating melt inclusion, pinches off (A) and converts into a trail of isolated fluid inclusions (B). (**C**) Transmitted-light microphotograph of an olivine crystal with several melt-and-bubble inclusions (run PdF1; see Table 1). Scale bars, 50 μm.

gives $V = f(\Delta\mu_T)$, where $\Delta\mu_T$ is proportional to $\theta$ and $L$. Depending on the dissolution and crystallization mechanism (continuous detachment and attachment, screw dislocation growth, or surface nucleation), $V$ is proportional to $\Delta\mu_T$, $(\Delta\mu_T)^2$, or $\exp(-a/\Delta\mu_T)$, and hence to $\theta L$, $\theta^2 L^2$, or $\exp(-b/\theta L)$ [where $b = 2a/(S^0_{liq} - S^0_{sol})$].

Some olivine crystals host several melt inclusions of different sizes (Fig. 2C). Subjected to the same thermal gradient, these inclusions migrate along parallel paths but at different speeds, serving as further evidence that chemical diffusion is not the rate-controlling process. Moreover, migration rate is proportional to inclusion length (Fig. 3B), which points to continuous detachment and attachment as the controlling mechanism at the interface. Finally, migration rates obtained for different crystals with different experimental conditions are plotted as a function of $\theta L$ in Fig. 3C: They define a single straight line running through the origin, which supports the kinetic law $V = k\theta L$ (i.e., continuous detachment and attachment). It also shows that the kinetic constant $k$ is not very sensitive to temperature or melt composition: $k \approx 0.5$ nm s$^{-1}$ K$^{-1}$. Notably, control by interface kinetics, not diffusion, has also been obtained for the thermal migration of brine droplets in synthetic halides (*16*) and natural ice (*17*, *18*).

That dissolution and crystallization are governed by continuous detachment and attachment may seem perplexing, given that continuous growth is usually associated with large local undercoolings (i.e., the difference between liquidus and actual temperatures at the interface) and nonfaceted shapes (*11*) and that it is explained by uniform face attachment (UFA) on rough interfaces. Actually, as discussed thoroughly by Tiller (*19*), two other continuous regimes exist at low undercoolings: uniform ledge attachment (ULA), when growth units can only attach onto the crystal at layer edges, and kink-only attachment (KOA), when they can join the crystal only at kink sites. Both apply to faceted shapes and are reversible (with the same constant $k$ applying to both dissolution and crystallization), and KOA at least applies down to zero driving force.

It is a classical result of crystal growth theory (*19*) that growth (or dissolution) rate control shifts from thermal and/or chemical diffusion at large bulk disequilibrium to interface kinetics at lower disequilibrium (of two processes acting in series, the slower process is in control). With decreasing disequilibrium at the interface, the governing interface-kinetics mechanism shifts from two-dimensional–island nucleation to screw dislocation growth to ULA to KOA (of several processes competing in parallel, the fastest is in control). Here, the bulk undercooling at rear (and overheating at front) reads $\Delta T = \theta L/2$. Our results show no dependence on $L$ (for a given $\Delta T$) and a linear dependence of growth (and dissolution) rates on $\Delta T$ for $\Delta T$ ranging from 1.6 down to 0.5 K (Fig. 3C). This observation and the evidence that KOA is normally valid down to zero undercooling allow us to extrapolate our results to the lower bulk undercoolings and therefore lower thermal gradients that apply in natural conditions, even if our experiments lie in the ULA regime ($k_{KOA} < k_{ULA}$, but they have the same order of magnitude).

This process of melt migration and associated fluid separation may have important implications. First, melt migration experiments permit the acquisition of basic quantitative data for crystal growth kinetics at bulk undercoolings <1 K. Such conditions are more appropriate to many natural systems [e.g., magma chambers (*20*)] than classical crystal growth experiments, which are generally done at large bulk undercoolings (tens of K) (*21*). Our experiments provide an unambiguous determination of a crystal-growth kinetic constant for a magmatic system, with no interference from nucleation delay, chemical diffusion, melt convection, or statistical hypotheses.

**Table 1.** Summary of melt migration experiments. $\bar{T}$ is mean temperature (maximum error $\delta$ = 5°C), $\theta$ is thermal gradient ($\delta$ = 5 mK/μm), $t_f$ is run duration ($\delta$ = 30 s), $L$ is inclusion length (measured at the end of experiment, $\delta$ = 0.5 μm), $l$ is final bubble track length ($\delta$ = 0.5 μm), $V$ is migration rate ($l/t_f$, $\delta$ = 0.5 nm/s). For crystals with several melt inclusions (runs Som2, Som5, and PdF1), the reported $L$, $l$, and $V$ stand for the longest. n.d., not determined.

| Run no. | $\bar{T}$ (°C) | $\theta$(K/μm) | $t_f$ (min) | $L$ (μm) | $l$ (μm) | $V$ (nm/s) |
|---|---|---|---|---|---|---|
| | | | *La Sommata (Vulcano Island)* | | | |
| Som1 | 1155 | 0.05 | 304 | 134 | 58 | 3.2 |
| Som2 | 1175 | 0.05 | 60 | 80 | 7 | 1.9 |
| Som3 | 1140 | 0.06 | 300 | 65 | 37 | 2.1 |
| Som4 | 1126 | 0.05 | 964 | n.d. | 55 | 1.0 |
| Som5 | 1134 | 0.04 | 403 | 85 | 37 | 1.5 |
| Som6 | 1170 | 0.03 | 362 | 100 | 36 | 1.7 |
| | | | *Piton Vincendo (Reunion Island)* | | | |
| PdF1 | 1190 | 0.04 | 180 | 73 | 14 | 1.3 |
| PdF2 | 1196 | 0.03 | 1200 | 30 | 19 | 0.3 |

Second, the separation of fluid inclusions from parent melt inclusions is relevant to Earth's mantle on geological time scales. Temperature and pressure are known to stimulate most reaction kinetics, but no systematic study is available for liquid-solid systems, so we use our experimental kinetic constant $k$ as a conservative estimate. Horizontal (*22*) and vertical (*23*, *24*) gradients on the order of 0.5 and 5 K/km, respectively, are known to prevail in the shallow continental mantle. Taking 5 K/km, complete melt-fluid separation is achieved in 25,000 years. Silicate melt and $CO_2$-rich fluid inclusions in olivines and pyroxenes of ultramafic xenoliths have already been recognized as cogenetic (*25*) (because of their systematic spatial association, the occurrence of multiphase inclusions, and that of melt inclusions and fluid inclusions joined by necks), but a physical explanation was lacking. The morphological resemblance of deformed, necking-down melt-and-fluid inclusions and rows of residual fluid inclusions in our experiments to dumbbell-shaped melt-and-fluid inclusions and fluid inclusion arrays commonly observed in mantle xenoliths (*1*) further suggests that the latter represent remnants of transcrystalline melt migration. If this interpretation is correct, little basis remains for the current hypothesis that fluid inclusions in mantle xenoliths are trapped samples of a free, deeply percolating fluid phase (*1*).

Third, transcrystalline melt migration provides a previously unrecognized mechanism for the grain-scale segregation of magma. Current models of thermal structure and flow field beneath mid-ocean ridges (*26*, *27*) and hot spots (*28*) predict gradients up to hundreds or thousands of K/km, locally. For a typical $SiO_2$-rich mantle melt inclusion 20 μm long (*25*), $\theta$ = 100 K/km translates into $V = 10^{-15}$ m/s; i.e., it migrates by 30 μm in 1000 years. This is faster than buoyancy-driven interconnected porous flow (*29*) for such viscous melts ($\eta \approx 3000$ Pa s) (*30*) at all melt fractions less than 0.1%. This may answer the questions as to why very primitive [less than 1% partial melting (*31*, *32*)] $SiO_2$-rich melts are only encountered as melt inclusions in mantle olivines (never as magma bodies), whereas less primitive (1 to 10% partial melting) basaltic melts are only encountered as magma bodies (never as melt inclusions in mantle olivines). Only the most primitive droplets formed at fertile grain corners (or edges) have time (if melting does not proceed rapidly to higher degrees) to enter the crystals by thermally driven migration, instead of escaping by buoyancy-driven flow along grain edges. Less primitive melts form interconnected wetted-edge networks and escape rapidly to higher levels where grain-scale channels are relayed by fracture networks [or chemically formed channels (*33*)] and collection into magma bodies.

**References and Notes**

1. E. Roedder, Ed., *Fluid Inclusions*, vol. 12 of *Reviews in Mineralogy* (Mineralogical Society of America, Washington, DC, 1984).
2. H. Bureau, F. Pineau, N. Metrich, M. Semet, M. Javoy, *Chem. Geol.* **147**, 115 (1998).
3. A. Gioncada *et al.*, *Bull. Volcanol.* **60**, 286 (1998).
4. D. Massare, N. Métrich, R. Clocchiatti, *Chem. Geol.* **183**, 87 (2002).
5. A. V. Sobolev, L. V. Dmitriev, V. L. Barsukov, V. N. Nevsorov, A. B. Slutsky, in *Igneous Processes and Remote Sensing,* vol. 11 of *Proceedings of the Lunar and Planetary Science Conference*, P. R. Criswell, R. B. Merrill, Eds. (Pergamon, New York, 1980), pp. 105–116.
6. P. Schiano, *Earth Sci. Rev.* **63**, 121 (2003).
7. B. J. Wanamaker, B. Evans, *Contrib. Mineral. Petrol.* **102**, 102 (1989).
8. D. B. Dingwell, K. U. Hess, C. Romano, *Earth Planet. Sci. Lett.* **158**, 31 (1998).
9. Y. Zhang, Z. Xu, Y. Liu, *Am. Mineral.* **88**, 1741 (2003).
10. W. A. Deer, R. A. Howie, J. Zussman, *Orthosilicates* (Longman, London, 1962).
11. A. Baronnet, *Fortschr. Miner.* **62**, 187 (1984).
12. L. C. Kuo, R. J. Kirkpatrick, *Am. J. Sci.* **285**, 51 (1985).
13. C. H. Donaldson, *Lithos* **8**, 163 (1975).
14. J. E. Mungall, C. Romano, D. B. Dingwell, *Am. Mineral.* **83**, 685 (1998).
15. D. Snyder, E. Gier, I. Carmichael, *J. Geophys. Res.* **99**, 15503 (1994).
16. D. R. Olander, A. J. Machiels, M. Balooch, S. K. Yagnik, *J. Appl. Phys.* **53**, 669 (1982).
17. H. E. Cline, T. R. Anthony, *J. Appl. Phys.* **43**, 10 (1972).
18. D. R. H. Jones, *J. Cryst. Growth* **20**, 145 (1973).
19. W. A. Tiller, *The Science of Crystallization: Microscopic Interfacial Phenomena* (Cambridge Univ. Press, Cambridge, UK, 1991).
20. G. Brandeis, C. Jaupart, C. J. Allègre, *J. Geophys. Res.* **89**, 10161 (1984).
21. R. J. Kirkpatrick, in *Reviews in Mineralogy vol 8*, A. C. Lasaga, R. J. Kirkpatrick, Eds. (Mineralogical Society of America, Washington, DC, 1981), pp. 321–398.
22. J. C. Mareschal, C. Jaupart, *Earth Planet. Sci. Lett.* **223**, 65 (2004).
23. S. V. Sobolev *et al.*, *Tectonophysics* **275**, 143 (1997).
24. N. M. Shapiro, M. H. Ritzwoller, J. C. Mareschal, C. Jaupart, in *Geological Prior Information: Informing Science and Engineering*, A. Curtis, R. Wood, Eds. (Geological Society of London Special Publication, London, 2004), vol. 239, pp. 175–194.
25. P. Schiano, R. Clocchiatti, *Nature* **368**, 621 (1994).
26. M. J. Cordery, J. P. Morgan, *J. Geophys. Res.* **98**, 19477 (1993).
27. Y. J. Chen, J. Lin, *Earth Planet. Sci. Lett.* **221**, 263 (2004).
28. C. G. Farnetani, B. Legras, P. J. Tackley, *Earth Planet. Sci. Lett.* **196**, 1 (2002).
29. T. J. Henstock, *Geophys. Res. Lett.* **29**, 1137 (2002).
30. J. Maumus, D. Laporte, P. Schiano, *Contrib. Mineral. Petrol.* **148**, 1 (2004).
31. P. Schiano *et al.*, *Earth Planet. Sci. Lett.* **160**, 537 (1998).
32. M. M. Hirschmann, M. B. Baker, E. M. Stolper, *Geochim. Cosmochim. Acta* **62**, 883 (1998).
33. E. Aharonov, J. A. Whitehead, P. B. Kelemen, M. Spiegelman, *J. Geophys. Res.* **100**, 20433 (1995).


34. We thank B. Thellier and D. Massare for technical assistance. Financial support was provided by the European Community's Human Potential Programme under contract HPRN-CT-2002-00211 (Euromelt).


**Supporting Online Material**
www.sciencemag.org/cgi/content/full/314/5801/970/DC1
Figs. S1 and S2
Tables S1 and S2
Reference


13 July 2006; accepted 10 October 2006
10.1126/science.1132485


# Selective Etching of Metallic Carbon Nanotubes by Gas-Phase Reaction


**Guangyu Zhang,* Pengfei Qi,* Xinran Wang, Yuerui Lu, Xiaolin Li, Ryan Tu, Sarunya Bangsaruntip, David Mann, Li Zhang, Hongjie Dai†**



**Metallic and semiconducting carbon nanotubes generally coexist in as-grown materials. We present a gas-phase plasma hydrocarbonation reaction to selectively etch and gasify metallic nanotubes, retaining the semiconducting nanotubes in near-pristine form. With this process, 100% of purely semiconducting nanotubes were obtained and connected in parallel for high-current transistors. The diameter- and metallicity-dependent "dry" chemical etching approach is scalable and compatible with existing semiconductor processing for future integrated circuits.**


Carbon nanotubes have shown promise for future electronics (*1–6*). However, a major roadblock to the scaling up of single-walled carbon nanotube (SWNT) field-effect transistors (FETs) has been the difficulty in obtaining purely semiconducting SWNTs (S-SWNTs) without electrical short by metallic SWNTs (M-SWNTs). Parallel S-SWNTs are necessary to enable high-current and high-speed nanotube FETs to surpass modern silicon devices. Various approaches have been developed for selective synthesis of S-SWNTs (*7*, *8*), electrical breakdown of M-SWNTs (*9*, *10*), solution-phase chemical separation (*11*, *12*) and selective chemical modification (*13–15*). For large-scale circuits, much remains to be done to achieve full semiconductor yield, high scalability of metallic SWNT removal, optimum nanotube diameter and length, and highly preserved electrical properties of SWNTs.

Here, we demonstrate a methane plasma followed by an annealing process to selectively hydrocarbonate M-SWNTs and retain S-SWNTs grown on substrates. The retained S-SWNTs are free of covalent alterations, are stable at high temperatures, and exhibit electrical properties similar to pristine materials. The distribution of diameters of the S-SWNTs is narrowed down to a window (~1.3 to 1.6 nm) that provides sufficient band gaps for high on/off ratios and allows for good electrical contacts (*16*), both of which are important in high-performance electronics. The dual effects of selective metal removal and diameter distribution narrowing combined with compatibility with microfabrication technology make the method promising for large-scale SWNT electronics.

We first fabricated an array (Fig. 1A) of 98 "few-tube" electrical devices on $SiO_2$(67 nm)/Si (as back-gate) (Fig. 1A, bottom) substrates, with each device comprising 0 to 3 as-grown SWNTs [by patterned chemical vapor deposition (CVD) growth (*17*) at 800°C] bridging source-drain (S-D) Ti/Au electrodes (S-D distance ~ 400 nm) (Fig. 1A). The particular CVD recipe produced SWNTs in a broad diameter ($d$) range of $d$ = 1 to 2.8 nm, measured by atomic force microscopy (AFM). About 55% of the as-fabricated devices (out of 244 measured on six chips) were found to be "depletable" (D) by sweeping gate-voltage with on/off conductance ratios $\geq 10^3$. These were devices fortuitously composed of one or multiple (two or three) as-grown S-SWNTs. The other 45% of the devices contained at least one M-SWNT (with or without S-SWNT) and were "nondepletable" (ND) with on/off ratios $\leq 10$.

We treated hundreds of as-made few-tube device arrays by exposure to a methane plasma at 400°C, followed by 600°C annealing in vacuum in a 4-inch quartz-tube furnace equipped with a remote plasma system (*18*). The use of methane plasma instead of hydrogen plasma was found key to selective M-SWNT etching because of milder reactivity and higher controllability. After the treatment, the percentage of depletable devices increased from ~55% (out of 244) to ~93% (out of 78 that survived), with only a few nondepletable devices remaining (Fig. 2A), indicating that selective removal of metallic SWNTs over semiconducting ones was occurring.

We observed five different behaviors with the 244 few-tube devices after the treatments, including ND→D (i.e., non-


Department of Chemistry and Laboratory for Advanced Materials, Stanford University, Stanford, CA 94305, USA.

*These authors contributed equally to this work.
†To whom correspondence should be addressed. E-mail: hdai@stanford.edu